Nanoscopic recombination processes in InGaN/GaN quantum wells emitting violet, blue, and green spectra

A. Kaneta,* M. Funato,† and Y. Kawakami‡
Department of Electronic Science and Engineering, Kyoto University, Kyoto 615-8510, Japan
(Received 21 May 2008; revised manuscript received 25 July 2008; published 16 September 2008)

We investigated correlations between nanoscopic optical and structural properties in violet-emitting, blue-emitting, and green-emitting $In_xGa_{1-x}N/GaN$ quantum wells (QWs) by means of scanning near-field optical microscopy (SNOM) and atomic force microscopy. Only in the blue-emitting QW, threading dislocations were not major nonradiative recombination centers (NRCs). SNOM data indicated that NRCs in the blue-emitting QW are surrounded by energy levels higher than those for radiative recombination. Such potential distributions realize "antilocalization" of carriers to NRCs, which is the cause of high emission quantum efficiencies in blue emitters.

DOI: 10.1103/PhysRevB.78.125317 PACS number(s): 78.67.De, 61.72.Lk, 68.37.Uv

I. INTRODUCTION

$In_xGa_{1-x}N$ has a high potential in producing light emitters such as light emitting diodes (LEDs) and laser diodes (LDs).[1] Because the band-gap energies of GaN and InN are 3.4 (Ref. 2) and 0.6 eV,[3] respectively, $In_xGa_{1-x}N$ covers the full visible spectral range, and in fact, violet to green LEDs and violet to blue LDs have already been commercialized using this material. In recent years, much progress has been made to improve the external quantum efficiency (EQE) of $In_xGa_{1-x}N$ LEDs. As a result, despite high threading dislocation densities (TDDs) due to epitaxial growth on highly mismatched sapphire substrates, to date, the maximum EQE value of 75.5% has been achieved for blue LEDs, which has led to the fabrication of white LEDs with a luminous efficacy of approximately 169 lm/W.[4] (It is noteworthy that this luminous efficacy is much greater than that of fluorescent lamps.) However, such a high efficiency is achieved only in the blue spectral band, and it tends to decrease outside this spectral range.[4,5] One interesting finding is that reducing TDD in underlying GaN templates effectively improves EQE in the ultraviolet (UV) to violet spectral range but does not work in the blue to green spectral range.[6] Apparently, threading dislocations (TDs) play a crucial role in determining carrier recombination dynamics in $In_xGa_{1-x}N$, but questions arise as to why TDs affect the emission quantum efficiency of only UV to violet emitters and why blue emitters exhibit the highest emission quantum efficiency in spite of comparable TDDs in UV to green emitters.

To answer those questions, nanoscopic optical and structural properties have been assessed by correlating the cathodoluminescence (CL) mapping with structural analyses in heteroepitaxial GaN layers grown on sapphire substrates[7–10] and in $In_xGa_{1-x}N$ QWs.[11–14] Two different mechanisms have been proposed on the relationship between three types of TDs (edge, screw, and mixed TDs) and nonradiative recombination centers (NRCs). The first one is that the screw-type and mixed-type TDs act as NRCs, excluding the role of the edge-type TDs.[7–9,11] The other one is that edge-type TDs as well as screw-type and mixed-type TDs act as NRCs.[10,12,14] However, CL cannot generate carriers selectively in the QWs, and thus, generated carriers in the cladding layers may be captured in part by TDs before reaching the QWs. Hence, in addition to the intrinsic nature in QWs, this process contributes to the dark spot image in the CL. Furthermore, although the electron-beam diameter can be reduced to less than 10 nm, carrier diffusion within the material worsens the spatial resolution.

On the other hand, scanning near-field optical microscopy (SNOM)[15–19] is advantageous over CL because of (1) selective photoexcitation in the well, (2) higher spatial resolution,[16,17] and (3) feasibility to time resolve measurements.[18,19] In addition, comparing images obtained from the illumination-collection (*I-C*) mode, which uses an identical fiber probe to excite and detect photoluminescence (PL), and those from the illumination (*I*) mode, which excites PL through a fiber and detects it in a far field, can provide insight into radiative recombination, nonradiative recombination, and diffusion processes.[19] Remarkably, we like to emphasize that visualization of diffusion processes is achievable solely by SNOM. A drawback of SNOM was a difficulty in correlating PL mapping to topography with keeping high spatial resolutions for both the measurements simultaneously. To circumvent this issue, we have developed an experimental technique to precisely superimpose SNOM-PL images onto AFM ones. This technique is based on reference metal markers formed on the sample surface. Here we applied this characterization technique hybridized from multimode SNOM, which can operate simultaneously in the *I-C* mode and *I* mode,[19] and AFM to 3-nm-thick violet-emitting, blue-emitting, and green-emitting $In_xGa_{1-x}N/GaN$ single quantum wells (SQWs) fabricated on epitaxially laterally overgrown (ELO) GaN, and investigated the carrier recombination processes in relation to the structural properties. All the measurements were performed at room temperature (RT).

II. EXPERIMENT

A. Fabrication

The samples used in this study were $In_xGa_{1-x}N$ SQWs grown by metalorganic chemical vapor deposition. First, 15-μm-thick ELO-GaN templates were prepared on sapphire

TABLE I. Sum of screw-type and mixed-type TDDs estimated from the number of pits observed by AFM measurements.

	Dislocation density (cm^{-2})	
	Wing	Seed
GaN template	$<1\times10^7$	2×10^8
Violet	$<1\times10^7$	2×10^8
Blue	$<1\times10^7$	2×10^8
Green	2×10^8	5×10^8

(0001) substrates. The SiO_2 mask for ELO-GaN had a stripe pattern composed of a repetition of the 4-μm-wide seed region and 16-μm-wide wing region. Then, a 3-μm-thick undoped GaN, a 3-nm-thick $In_xGa_{1-x}N$ SQW, and a 5-nm-thick undoped GaN cap layer were subsequently grown. The macroscopic PL peaks of the samples were located at about 400 (violet), 470 (blue), and 520 nm (green) at RT, which corresponded to the In compositions of 8%, 20%, and 25%, respectively. The densities of the sum of screw-type and mixed-type TDs obtained by AFM measurements for the GaN template, violet-emitting, blue-emitting, and green-emitting SQWs are summarized in Table I.

B. SNOM measurements

PL mapping was performed at RT with the SNOM system, which was developed at Kyoto University by modifying NFS-300 (JASCO Corp.). The excitation wavelength, type of the fiber probe, and aperture diameter for each measurement are summarized in Table II. The excitation lasers were coupled with fibers and illuminated the samples through the fiber probes. It is noteworthy that the $In_xGa_{1-x}N$ active layers were selectively photoexcited in all the measurements. The mean carrier density under those excitation conditions were estimated to be about 1×10^{17} cm^{-3}. The exciton stability with respect to the carrier density has been studied in InGaN,[20,21] GaN,[21–24] and AlGaN.[25,26] According to these reports, the carrier density in our experiments was low enough for excitons to survive. In the *I-C* mode, the PL signal was collected by the same fiber probe to exclude the effect of carrier and/or exciton diffusions. In the *I* mode, the PL signal was collected by a lens in a far field from the backside of sample. The collected PL signals were introduced into a monochromator ($f=50$ cm) in conjunction with a cooled charge coupled device (CCD) detector (Roper Scientific, Spec-10:100B/LN) so that our system could acquire a PL spectrum at each measuring point. In order to compare exactly the SNOM-PL image and AFM image, we introduced reference metal markers formed by photolithography and lift-off methods. The marker was a Ni/Au multilayer, of which the height and width were 50 nm and 10 μm, respectively. The markers were located at the four corners of a 20×20 μm^2 square so that the observing area is equivalent to one period of the ELO mask stripes.

III. ROLE OF TDS

Generally, GaN heteroepitaxial layers involve three types of TDs, which are edge-type, screw-type, and mixed-type TDs. They appear as growth pits in AFM images. The screw-type and mixed-type TDs are always located at the growth steps[27] and have large cores to be detected by AFM. Therefore, although they were indistinguishable from each other by AFM, their positions were clearly identified. On the other hand, the core of the edge-type TD is too small to be detected in large area AFM images similar to those in the figures below. Hence, we performed a high-resolution AFM mapping in a smaller area for a GaN template, by which the ratio of the edge-type TDD against the density of the sum of screw-type and mixed-type TDs was determined to be ~7. This ratio depends on sample details such as growth conditions and impurity doping, and for example, Hino *et al.*[7] reported a factor of ~10. Therefore, we precisely estimated the screw-type and mixed-type TDDs from the growth pits revealed by AFM as summarized in Table I, whereas we roughly estimated the edge-type TDD from the ratio of 7–10.

Figure 1 shows the SNOM-PL intensity mappings in the *I-C* mode, AFM images, and PL intensity profiles of violet-emitting, blue-emitting, and green-emitting SQWs. The PL intensity profiles were obtained by averaging the SNOM-PL intensities along the ELO mask stripes. The averaged PL intensities were normalized by those in the wing regions. The open circles in the SNOM images [Figs. 1(b), 1(e), and 1(h)] indicate growth pits observed in the corresponding AFM images [Figs. 1(a), 1(d), and 1(g)]. Those pits were screw-type and mixed-type TDs, as mentioned above.

For the violet-emitting QW, comparison between the SNOM [Fig. 1(b)] and AFM [Fig. 1(a)] images confirmed that these screw-type and mixed-type TDs correspond well to the dark area in the SNOM-PL mapping in the seed region for the ELO growth. Moreover, the averaged PL intensity [Fig. 1(c)] of the seed region was about 0.78 times as weak as that of the wing region. These results directly evidence that these TDs act as NRCs in the violet-emitting QW. How-

TABLE II. Summary of SNOM measurement conditions.

	Violet	Blue		Green	
Excitation wavelength (nm)	370	400		400	
Fiber-type	Pure SiO_2	GeO_2 doped SiO_2		GeO_2 doped SiO_2	
Probe structure	Single taper	Double taper		Double taper	
Aperture diameter (nm)	*I-C* mode	*I-C* mode	Multimode mode	*I-C* mode	Multimode mode
	160	70	160	120	260

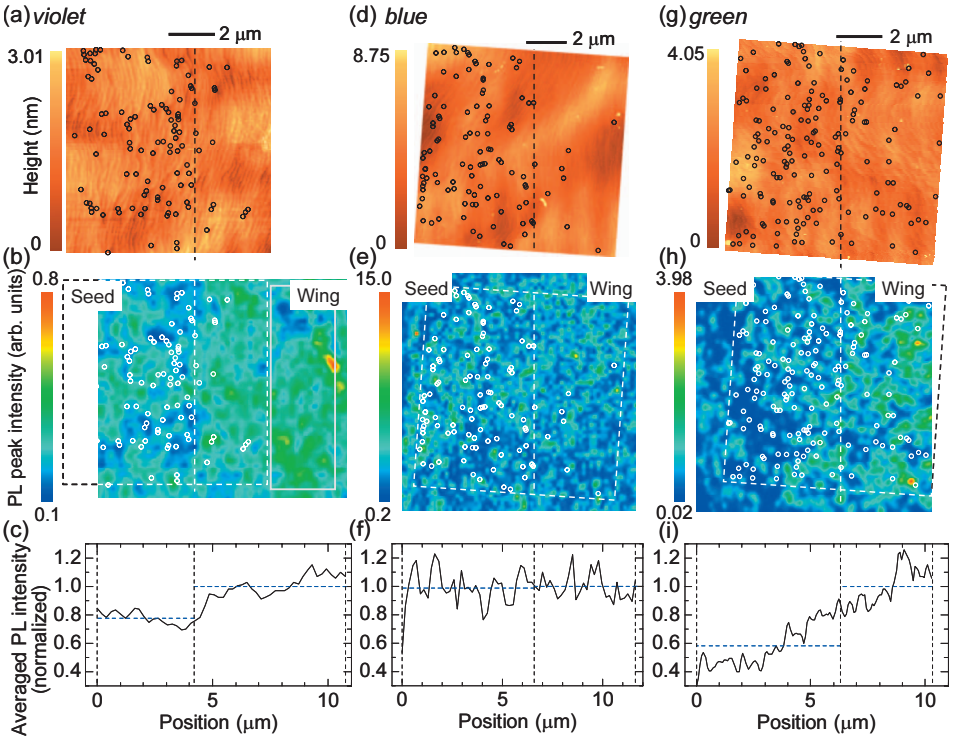

FIG. 1. (Color) AFM images [(a), (d), and (g)], SNOM PL mappings in the *I-C* mode [(b), (e), and (h)], and spatially averaged PL intensity profiles [(c), (f), and (i)] of the violet-emitting, blue-emitting, and green-emitting $In_xGa_{1-x}N$ SQWs. (a), (b), and (c) are for the violet-emitting SQW; (d), (e), and (f) are for the blue-emitting SQW; and (g), (h), and (i) are for the green-emitting SQW. Dotted squares in the SNOM images indicate the areas scanned by AFM.

ever, the PL intensity fluctuated even in the wing region, although these types of TDs were only sparsely observed in the vicinity of the border between the seed and wing regions, and were nearly undetectable when the area was more than a few micrometers away from the border. Regarding the edge-type TD, it is difficult at this stage to correlate it with either radiative recombination centers (RRCs) or NRCs because its location cannot be identified in this large area AFM image. However, their number in the area surrounded by the white square in Fig. 1(b) was estimated to be less than 10. These results led us to a conclusion that the considerable PL intensity fluctuations in the wing region are not due to any types of TDs but due to spatial clustering of nanoscopic point defects related to other types of NRCs such as vacancies, interstitials, antisite defects, and their complexes.[28]

Unlike the violet-emitting QW, the blue-emitting QW did not show correlations between the TD distribution [Fig. 1(d)] and the PL intensity distribution [Fig. 1(e)]. Furthermore, the spatially averaged PL intensities [Fig. 1(f)] were almost unchanged in both regions. These results indicate that the TDs hardly contribute to recombination dynamics as NRCs in the blue-emitting $In_xGa_{1-x}N$ SQW and two conclusions can be extracted: one is that the area rich in point defects and vacancies should be the main origin of the dark PL domains and the other is that the diffusion length of the carriers is too short to be captured at the core region of the TDs probably due to the large potential fluctuations, which is discussed below in more detail.

The green-emitting QW strikingly contrasted the blue-emitting QW. As can be estimated from Fig. 1(g), the TDD of the green-emitting QW became one order of magnitude higher than those in other QWs as well as the underlying ELO-GaN templates. Consequently, the TD distribution clearly correlated with the SNOM-PL image [Fig. 1(h)] and the spatially averaged PL intensity [Fig. 1(i)] of the seed region was about 0.58 times as weak as that of the wing region. Furthermore, although step and terrace structures were observed [Fig. 1(g)], undulation of their edges induced by the spiral growth was more pronounced. It is thus obvious that new TDs were generated during the QW growth. There are two possible mechanisms responsible for this; one is a lowered growth temperature for reaching higher In incorporations[29] and the other is the critical layer thickness (CLT) of $In_xGa_{1-x}N$ on GaN. The CLT, which decreases as the In composition increases, was calculated to be 4 nm for $In_{0.3}Ga_{0.7}N$ based on the model developed by Fisher *et al.*[30] Because this CLT is comparable to the well thickness of 3 nm, partial lattice relaxation may happen to create TDs. At present, no further conclusion can be reached before doing, for example, transmission electron microscopy measurements.

Because PL spectra were acquired during the SNOM measurements, the PL intensity mapping shown in Fig. 1 can

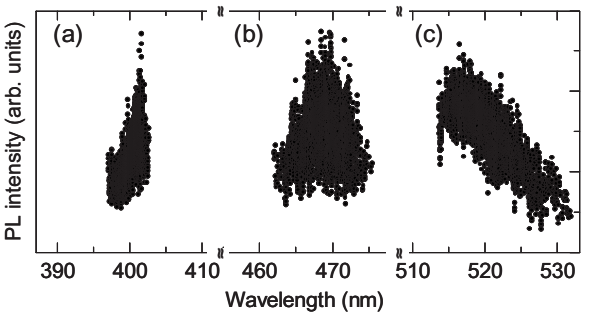

FIG. 2. Relationship between PL peak intensity and wavelength of the (a) violet, (b) blue, and (c) green-emitting $In_xGa_{1-x}N$ SQWs. Local PL intensity was probed by SNOM in the *I-C* mode.

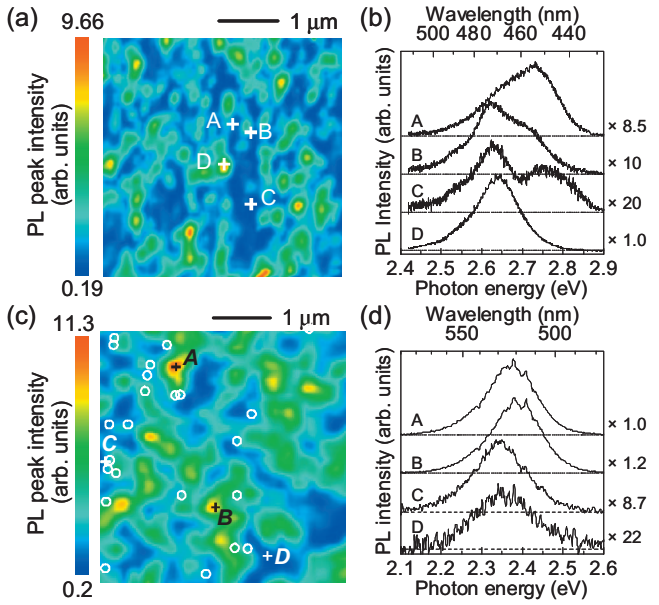

FIG. 3. (Color) (a) SNOM image in the *I*-*C* mode and (b) PL spectra taken at positions A to D in the wing region of the blue-emitting SQW. (c) and (d) are those for the green-emitting SQW.

directly be correlated with the PL peak wavelength mapping. Thus, Fig. 2 plots the PL intensity in the *I*-*C* mode as a function of the emission wavelength. An inverse V-shape correlation was clearly observed, which can be interpreted as follows by considering the results of Fig. 1. When the In composition is small like in the violet-emitting QW, carriers can easily diffuse from the probing area (to be captured by TDs) due to small potential fluctuations. Then, increasing the In composition enhances potential fluctuations and suppresses carrier diffusion to TDs. Consequently, the PL intensity increases with increasing emission wavelength. This trend continues up to ~470 nm in the blue-emitting QW. Further increase in the In composition newly generates TDs as NRCs, and the PL intensity decreases with increasing emission wavelength.

IV. POTENTIAL FLUCTUATIONS IN InGaN QWS

The previous section suggested that potential fluctuations in $In_xGa_{1-x}N$ are an important factor to determine the sensitivity of carriers to dislocations. To clarify potential distributions, the SNOM-PL intensity mapping and local PL spectra were examined in more detail.

Figure 3 displays typical results of the SNOM-PL intensity mappings in the *I*-*C* mode and the PL spectra for the blue-emitting QW [Figs. 3(a) and 3(b), respectively] and the green-emitting QW [Figs. 3(c) and 3(d), respectively]. The PL spectra were acquired at positions A, B, C, and D marked in the respective SNOM images. The data shown are for the wing regions of the ELO growth. No growth pits were observed by AFM within Fig. 3(a) due to the reduction in TDDs by the ELO technique. In contrast, in Fig. 3(c), although the TDDs were reduced by the ELO technique, 23 growth pits, which are indicated by open circles, were observed in the AFM measurement. The numbers of the edge-type TDs are supposed to be <30 in Fig. 3(a) and <200 in Fig. 3(c), respectively.

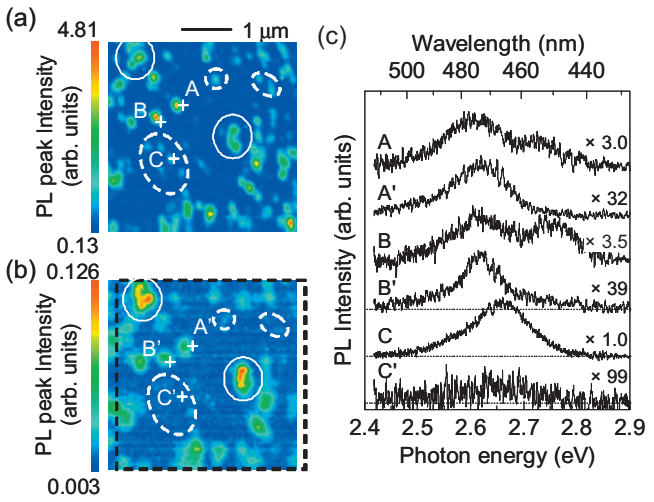

FIG. 4. (Color) SNOM images in (a) the *I*-*C* mode and (b) the *I* mode. Images were taken in the seed region. (c) PL spectra observed at positions designated by A to C in (a) [or equivalently, A′ to C′ in (b)].

For the blue-emitting QW [Figs. 3(a) and 3(b)], it was found that the PL spectra taken at the dark area (C) or at boundary between bright and dark area (A and B) were composed of double emission peaks, independent of the existence of dislocations, whereas those taken at the bright area (D) were composed of a single emission peak. The observed features of the PL intensity distribution in the seed region were nearly the same, despite the larger TDDs, and intense PL islands with a diameter of about 200 nm were surrounded by dark areas. Furthermore, the feature of the PL spectra was also the same in both regions. These findings suggest that NRCs are strongly related to point defects, which cannot be detected by AFM, and that the potential energy around NRCs

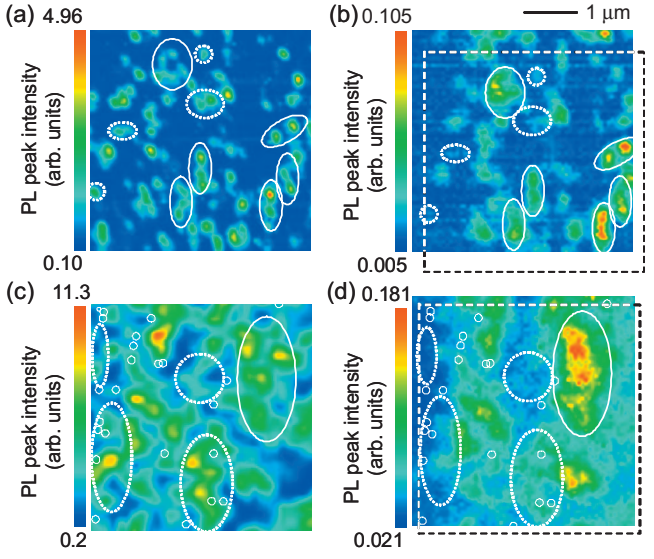

FIG. 5. (Color) (a) SNOM image in the *I*-*C* mode and (b) that in the *I* mode of the blue-emitting SQW. (c) and (d) are those for the green-emitting SQW. Images were taken in the wing region.

is higher than that around the area rich in RRCs, which prevent carriers and/or excitons from being captured by NRCs.

On the other hand, for the green-emitting QW, Fig. 3(d) shows the PL spectra at positions A, B, C, and D. A and B represent strong PL positions, while C and D show weak PL ones. It was found that all the PL spectra were composed of a single emission peak, and that the PL peak wavelengths of the dark area (C and D) were longer than those of bright area (A and B). Such characteristics are not by chance but are reproducible in other monitored positions. Therefore, we presumed that areas with lower potential are associated with TDs and/or point defects so that carrier localization enhances the pathway to NRCs in the green-emitting QW.

V. CARRIER DIFFUSION IN InGaN QWS

To investigate carrier diffusion processes under the presence of potential fluctuations, we performed multimode SNOM-PL measurements. Let us begin by discussing the blue-emitting QW. Figure 4 shows (a) the spatial distribution of the PL intensity of the seed region in the *I-C* mode, (b) that in the *I* mode taken in the same scanning area, and (c) the PL spectra at positions A (A′), B (B′), and C (C′) in Figs. 4(a) and 4(b). All positions were selected to be boundaries between bright and dark areas. The PL spectra at positions A and B were composed of double emission peaks in the *I-C* mode, whereas those at positions A′ and B′ in the *I* mode showed a single emission peak, which was located on the low-energy side of the PL in the *I-C* mode, as shown Fig. 4(c). This result strongly suggests that regions with high and low band-gap energies are formed in the vicinity of the PL intensity boundary and that photogenerated carriers very effectively diffuse to the low band-gap region. Comparing the two SNOM images showed two types of dissimilarities. The first type is that the weak PL in the *I-C* mode becomes strong in the *I* mode, as indicated by the white circles in Figs. 4(a) and 4(b). In such areas, the carriers and/or excitons that are photogenerated directly under the aperture of the fiber probe are diffused and captured into localization states beyond the fiber aperture, and they recombine radiatively. The second type is opposite, where the PL intensity in the *I-C* mode is stronger than that in the *I* mode, as indicated by the dashed white circles, a representative of which is shown by C and C′ in Fig. 4. In these areas, the localization centers are closely coupled to NRCs affecting the emission quantum efficiency, and PL double peaks are no longer observable. Because almost the same features are also observed in the wing region as later shown in Fig. 5, the important conclusion is that any types of TDs barely influence the recombination processes in the blue-emitting $In_xGa_{1-x}N$ QWs.

The diffusion lengths of the carriers and/or excitons to NRCs and RRCs can be estimated from the cross-sectional profiles of the PL intensity mapping. The procedure to extract diffusion lengths has been detailed in Ref. 19. As mentioned above, there are two types of PL intensity variations between images obtained in the *I-C* and *I* modes; strong PL intensity islands in the *I-C* mode mapping become weak in the *I* mode mapping and vice versa. The former suggests diffusion into the area rich in NRCs, for which the diffusion length is defined as the half-width at half maximum (HWHM) evaluated by fitting the cross-sectional PL intensity profile obtained in the *I-C* mode with a Gaussian distribution. In contrast, the latter suggests diffusion into the area rich in RRCs, for which the diffusion length is determined by subtracting HWHM of the PL intensity profile in the *I-C* mode from that in the *I* mode. Averaging diffusion lengths obtained from ten different profiles, the representative diffusion lengths to NRCs and RRCs were estimated to be 80 and 30 nm, respectively, regardless of the monitoring regions (wing or seed). These values are substantially shorter than the average distance between TDs, and this is why a clear correlation was not observed between dark PL spots and TDs in the blue $In_xGa_{1-x}N$ SQW with this spatial resolution.

As shown in Figs. 3(b) and 4(c), the PL spectra taken in the *I-C* mode around boundaries between bright and dark PL domains were often composed of double emission peaks with an energy separation of about 130 meV. In order to discuss the origin of this energy separation, we calculated the transition energies under the influence of two factors: the QW thickness fluctuation and the In compositional fluctuation.[31] The nominal QW thickness and In composition were 3 nm and 20%, respectively. The AFM image of the sample surface consisted of one monomolecular layer (ML) steps and terraces as shown in Fig. 1(d), implying an atomically flat interface. However, an only 2.3 ML thickness fluctuation induces a difference in quantized energy levels of 130 meV. On the other hand, In compositional differences of 17% and 20% also lead to an energy difference of 130 meV. It should be noted that Hangleiter *et al.*[32] reported that the V-shape defects formed at the TDs act as negative localization centers, which lead to a dislocation-insensitive PL property due to the locally thin QWs around the defects. Therefore, it is not clear at present stage whether the variation of well layer thickness (order of a few MLs) or In compositional fluctuation contributes to the observed energy separation.

In order to clarify the differences of carrier diffusion and recombination dynamics in blue-emitting and green-emitting QWs, multimode SNOM-PL measurements were performed in the wing regions for both the QWs, as shown in Fig. 5. The *I-C* and *I* modes were taken at the same area. The thick white circles represent where the PL intensity domains in the *I-C* mode were spread in the *I* mode, while the white dashed circles represent the opposite tendency. Comparing the green-emitting QW [Figs. 5(c) and 5(d)] with the blue-emitting QW [Figs. 5(a) and 5(b)], it was found that the area designated by the dashed circles increased in the green-emitting QW. This observation suggests that in the green-emitting QW, carriers are easily diffused from the aperture due to the potential fluctuation, and then, many of them recombine nonradiatively due to the trapping at NRCs. Although the diffusion length was highly anisotropic and fluctuated in the randomly localized system, it appears to be a few hundred nanometer long, especially at the border of the intensity domains. This diffusion length is much longer than those in the blue-emitting QW discussed above, probably because of a longer recombination lifetime due not only to the piezoelectric effect[33,34] but also to the smaller localized RRCs[35] in the green-emitting QW. It is noteworthy that such

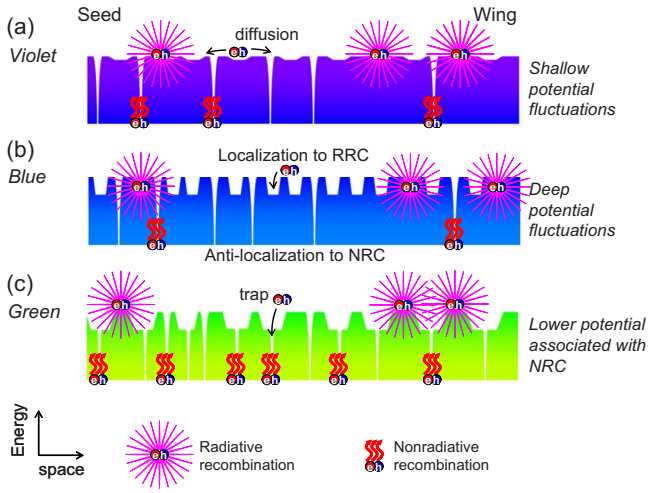

FIG. 6. (Color online) Schematic of local carrier recombination mechanism of the (a) violet-emitting, (b) blue-emitting, and (c) green-emitting $In_xGa_{1-x}N$ SQWs.

dark PL domains observed in the *I* mode correlate much better with TDs than those in the *I-C* mode.

Figure 6 is a schematic summary of the current study. In the violet-emitting QW, less potential fluctuations enhance carrier diffusion, and consequently, PL intensity mapping is well correlated with TD distribution. In the blue-emitting QW with a higher In composition, potential fluctuations are pronounced to affect carrier recombination processes in two different ways. One is carrier localization to RRCs as supported by a short carrier diffusion length and the other is carrier antilocalization to NRCs including TDs, as supported by the variation observed between SNOM-PL spectra in the *I-C* and *I* modes. This antilocalization effect is realized because NRCs are surrounded by energy levels higher than those for radiative recombination. In the green-emitting QW, further increase in the In composition in the InGaN well causes the introduction of TDs. In addition, longer recombination lifetimes elongate carrier diffusion length. As a result, many of the carriers recombine nonradiatively before reaching RRCs. Those observations lead us to a conclusion that $In_xGa_{1-x}N$ blue emitters can exhibit such high emission quantum efficiencies owing to localization to RRCs and antilocalization to NRCs, which are difficult to be simultaneously realized in other spectral ranges. Finally, we like to point out that the results of the green-emitting QW encourage the use of nonpolar or semipolar QWs because much faster radiative recombination processes are expected to suppress carrier trapping to NRCs and, consequently, to realize improvement of emission quantum efficiencies.

VI. CONCLUSION

The carrier recombination processes in violet-emitting, blue-emitting, and green-emitting $In_xGa_{1-x}N$ SQWs were elucidated by assessing the same surface area with multimode SNOM and AFM. The violet-emitting and green-emitting QWs clearly showed that TDs act as NRCs, whereas such correlation was not found for the blue-emitting QW. For the blue-emitting QW, NRCs are surrounded by energy levels higher than those for RRCs. Such potential fluctuations realize antilocalization of carriers to NRCs, which is, we consider, why InGaN blue emitters exhibit such high emission quantum efficiencies. For the green-emitting QW, weak PL was observed in the area emitting at lower-energy bands. These results indicate that many of carriers recombine nonradiatively before reaching RRCs.

ACKNOWLEDGMENTS

The authors would like to acknowledge Y. Narukawa and T. Mukai at Nichia Corporation for providing the SQW samples, and Y. Narita at JASCO Corporation for contributing the SNOM setup. This work was partially supported by the Kyoto University Venture Business Laboratory Project and by a Grant-in-Aid for Scientific Research from the Ministry of Education, Culture, Sports, Science and Technology, Japan.

*akio.kaneta@optomater.kuee.kyoto-u.ac.jp
†funato@kuee.kyoto-u.ac.jp
‡kawakami@kuee.kyoto-u.ac.jp

[1] S. Nakamura, S. Pearton, and G. Fasol, *Blue Laser Diode*, 2nd ed. (Springer, Heidelberg, 2000).
[2] B. Monemar, Phys. Rev. B **10**, 676 (1974).
[3] Y. Ishitani, H. Masuyama, W. Terashima, M. Yoshitani, N. Hashimoto, S. B. Che, and A. Yoshikawa, Phys. Status Solidi C **2**, 2276 (2005).
[4] Y. Narukawa, M. Sano, M. Ichikawa, S. Minato, T. Sakamoto, T. Yamada, and T. Mukai, Jpn. J. Appl. Phys., Part 2 **46**, L963 (2007).
[5] M. R. Krames, O. B. Shchekin, R. Mueller-Mach, G. O. Mueller, L. Zhou, G. Harbers, and M. G. Craford, J. Disp. Technol. **3**, 160 (2007).
[6] T. Mukai and S. Nakamura, Jpn. J. Appl. Phys., Part 1 **38**, 5735 (1999).
[7] T. Hino, S. Tomiya, T. Miyajima, K. Yanashima, S. Hashimoto, and M. Ikeda, Appl. Phys. Lett. **76**, 3421 (2000).
[8] S. J. Rosner, E. C. Carr, M. J. Ludowise, G. Girolami, and H. I. Erikson, Appl. Phys. Lett. **70**, 420 (1997).
[9] T. Sugahara, H. Sato, M. Hao, Y. Naoi, S. Kurai, S. Tottori, K. Yamashita, K. Nishino, L. T. Romano, and S. Sakai, Jpn. J. Appl. Phys., Part 2 **37**, L398 (1998).
[10] T. Miyajima, T. Hino, S. Tomiya, K. Yanashima, H. Nakajima, Y. Nanishi, A. Satake, Y. Masumoto, K. Akimoto, T. Kobayashi, and M. Ikeda, Phys. Status Solidi B **228**, 395 (2001).
[11] T. Sugahara, M. Hao, T. Wang, D. Nakagawa, Y. Naoi, K. Nishino, and S. Sakai, Jpn. J. Appl. Phys., Part 2 **37**, L1195 (1998).
[12] D. Cherns, S. J. Henley, and F. A. Ponce, Appl. Phys. Lett. **78**, 2691 (2001).

[13] S. Sonderegger, E. Feltin, M. Merano, A. Crottini, J. F. Carlin, R. Sachot, B. Deveaud, N. Grandjean, and J. D. Ganière, Appl. Phys. Lett. **89**, 232109 (2006).
[14] J. C. Brooksby, J. Mei, and F. A. Ponce, Appl. Phys. Lett. **90**, 231901 (2007).
[15] T. Saiki, K. Nishi, and M. Ohtsu, Jpn. J. Appl. Phys., Part 1 **37**, 1638 (1998).
[16] K. Matsuda, T. Saiki, S. Nomura, M. Mihara, and Y. Aoyagi, Appl. Phys. Lett. **81**, 2291 (2002).
[17] A. Kaneta, K. Okamoto, Y. Kawakami, G. Marutsuki, Y. Narukawa, T. Mukai, and Sg. Fujita, Appl. Phys. Lett. **81**, 4353 (2002).
[18] M. Ono, K. Matsuda, T. Saiki, K. Nishi, T. Mukaiyama, and M. Kuwata-Gonokami, Jpn. J. Appl. Phys., Part 2 **38**, L1460 (1999).
[19] A. Kaneta, T. Mutoh, G. Marutsuki, Y. Narukawa, T. Mukai, Y. Kawakami, and Sg. Fujita, Appl. Phys. Lett. **83**, 3462 (2003).
[20] D. Hirano and Y. Kanemitsu, J. Lumin. **128**, 712 (2008).
[21] D. Hirano, T. Tayagaki, and Y. Kanemitsu, Phys. Rev. B **77**, 073201 (2008).
[22] F. Binet, J. Y. Duboz, J. Off, and F. Scholz, Phys. Rev. B **60**, 4715 (1999).
[23] S. Hess, R. A. Taylor, K. Kyhm, J. F. Ryan, B. Beaumont, and P. Gibart, Phys. Status Solidi B **216**, 57 (1999).
[24] T. Nagai, T. J. Inagaki, and Y. Kanemitsu, Appl. Phys. Lett. **84**, 1284 (2004).
[25] P. Bigenwald, A. Kavokin, B. Gil, and P. Lefebvre, Phys. Rev. B **61**, 15621 (2000).
[26] P. Bigenwald, A. Kavokin, B. Gil, and P. Lefebvre, Phys. Rev. B **63**, 035315 (2001).
[27] D. Kapolnek, X. H. Wu, B. Heying, S. Keller, B. P. Keller, U. K. Mishra, S. P. DenBaars, and J. S. Speck, Appl. Phys. Lett. **67**, 1541 (1995).
[28] S. Chichibu, A. Uedono, T. Onuma, T. Sota, B. A. Haskell, S. P. DenBaars, J. S. Speck, and S. Nakamura, Appl. Phys. Lett. **86**, 021914 (2005).
[29] M. Hansen, P. Fini, M. Craven, B. Heying, J. S. Speck, and S. P. DenBaars, J. Cryst. Growth **234**, 623 (2002).
[30] A. Fischer, H. Kühne, and H. Richter, Phys. Rev. Lett. **73**, 2712 (1994).
[31] T. Takeuchi, H. Amano, and I. Akasaki, Jpn. J. Appl. Phys., Part 1 **39**, 413 (2000).
[32] A. Hangleiter, F. Hitzel, C. Netzel, D. Fuhrmann, U. Rossow, G. Ade, and P. Hinze, Phys. Rev. Lett. **95**, 127402 (2005).
[33] F. Bernardini, V. Fiorentini, and D. Vanderbilt, Phys. Rev. B **56**, R10024 (1997).
[34] A. Hangleiter, J. S. Im, H. Kolmer, S. Heppel, J. Off, and F. Scholz, MRS Internet J. Nitride Semicond. Res. **3**, 15 (1998).
[35] M. Funato and Y. Kawakami, J. Appl. Phys. **103**, 093501 (2008).